

# The large-scale frozen-in anticyclone in the 2011 Arctic summer stratosphere

Douglas R. Allen,<sup>1</sup> Anne R. Douglass,<sup>2</sup> and Susan E. Strahan<sup>3</sup>

Received 19 October 2012; revised 5 February 2013; accepted 6 February 2013; published 22 March 2013.

[1] The 2011 Arctic stratospheric final warming was characterized by a large-scale frozen-in anticyclone (FrIAC) that rapidly displaced the winter polar vortex, establishing unusually strong polar easterlies. A comprehensive overview of the 2011 FrIAC is provided using meteorological analyses, Microwave Limb Sounder (MLS) N<sub>2</sub>O observations, and N<sub>2</sub>O simulations from the Global Modeling Initiative (GMI) 3-D chemistry and transport model and the Van Leer Icosahedral Triangular Advection (VITA) 2-D (latitude × longitude) isentropic transport model. A vortex edge diagnostic is used to determine the FrIAC boundary, allowing quantification of several FrIAC properties. The 2011 FrIAC originated over North Africa in late March and traveled eastward and poleward over 2 weeks, forming a strong anticyclone that extended from ~580–2100 K potential temperature (~25–50 km). Low potential vorticity (PV) was transported to the pole with the FrIAC in early April; during May, most of the PV signature decayed due to diabatic processes. A small remnant negative PV anomaly persisted near the pole until mid-June. Tracer equivalent latitude was low initially and remained low throughout the summer. GMI, VITA, and MLS showed elevated N<sub>2</sub>O in the FrIAC, although the peak value was smaller in GMI due to a subtropical low bias. The high-resolution (~20 km) VITA filamentary structure quantitatively matched most of the features observed by MLS when smoothed to match the MLS resolution. The high-N<sub>2</sub>O anomaly persisted in the middle stratosphere over 4 months until late August, when it was destroyed by horizontal and vertical shearing, combined with photochemical processes.

**Citation:** Allen, D. R., A. R. Douglass, and S. E. Strahan (2013), The large-scale frozen-in anticyclone in the 2011 Arctic summer stratosphere, *J. Geophys. Res. Atmos.*, 118, 2656–2672, doi:10.1002/jgrd.50256.

## 1. Introduction

[2] The seasonal cycle of the Arctic extratropical stratospheric circulation is characterized by a strong winter polar vortex with cyclonic (westerly) circulation about the pole, reversing during the stratospheric final warming (SFW) to a weaker summer polar vortex with anticyclonic (easterly) circulation. This winter-to-summer transition produces persistent spatial structures in dynamical fields (e.g., potential vorticity (PV) or potential temperature) and long-lived trace gases (tracers) in the summer vortex [Hess, 1991]. The signature in the dynamical fields tends to decay on a timescale of 1–2 months due to diabatic processes, whereas anomalies in long-lived chemical tracers (e.g., nitrous oxide) can last much longer, persisting even until late August [Hess, 1990, 1991; Orsolini, 2001]. These features are said to be “frozen-in” to the summer easterly jet, which is characterized by weak horizontal and vertical shear [Piani and Norton, 2002], thereby allowing complicated structures to

remain unmixed for long time periods. The rather quiescent summer polar vortex can be contrasted with the Arctic winter polar vortex, in which large-scale irreversible mixing may occur in the presence of upward propagating Rossby waves [McIntyre and Palmer, 1983]. The summer easterlies effectively block the upward propagation of these waves [Charney and Drazin, 1961] and the flow becomes nearly zonally symmetric.

[3] A new class of polar anomaly that has been documented in recent years is the so-called frozen-in anticyclone (FrIAC), a long-lived anticyclone originating from low latitudes. FrIACs are unusual geophysical events in which low latitude air becomes trapped in traveling anticyclones that move to the polar region around the time of the SFW. The dynamical signature of the anticyclones decays due to diabatic processes, but the tracer anomalies accompanying them can persist through the entire summer, circling westward around the pole until late August. Allen *et al.* [2011] discussed the FrIAC life cycle in terms of a “spin-up phase” in which the anticyclone develops and moves to the polar region, an “anticyclonic phase” in which the anticyclone, along with an embedded tracer anomaly, gets trapped in the developing easterly polar vortex, and a “shearing phase” in which the anticyclone decays and the tracer anomaly is sheared out by the ambient wind. FrIAC formation has some similarities to low-ozone pocket (LOP) formation, in which low-latitude air is drawn into a developing anticyclone and

<sup>1</sup>Remote Sensing Division, Naval Research Laboratory, Washington, District of Columbia, USA.

<sup>2</sup>NASA Goddard Space Flight Center, Greenbelt, Maryland, USA.

<sup>3</sup>Universities Space Research Association, Columbia, Maryland, USA.

Corresponding author: D. R. Allen, Remote Sensing Division, Naval Research Laboratory, Washington, DC, USA. (Douglas.Allen@nrl.navy.mil)

©2013. American Geophysical Union. All Rights Reserved.  
2169-897X/13/10.1002/jgrd.50256

isolated from surrounding air, resulting in chemical ozone loss [Harvey *et al.*, 2008, and references therein]. However, while LOP signatures disappear with the decay of the anticyclone, the air within the FrIACs becomes enveloped into the summer circulation, resulting in unusual composition of the summer polar vortex that can have a strong influence on photochemical processes such as summertime ozone loss [Adams *et al.*, 2013].

[4] To date, four FrIACs have been identified using satellite observations of long-lived trace gases. These occurred in the spring/summer of 2003 [Lahoz *et al.*, 2007], 2005 [Manney *et al.*, 2006; Allen *et al.*, 2011], 2007 [Thiéblemont *et al.*, 2011], and 2011 [Allen *et al.*, 2012; Adams *et al.*, 2013]. The conditions necessary for FrIAC development were analyzed by Thiéblemont *et al.* [2011], who argued that FrIAC occurrence is more likely in years with no major winter sudden stratospheric warming and with tropical quasi-biennial oscillation easterly phase. Allen *et al.* [2012] further established a correlation between the strength of easterly winds following the final stratospheric warming and FrIAC-like signatures in long-lived tracers, suggesting that rapid wind reversal to strong easterlies is necessary to maintain the tracer anomaly. The four FrIACs that have been observed with satellite trace gas data were put into broader context by Allen *et al.* [2012] using a 33-year tracer equivalent latitude (TrEL) simulation. This analysis revealed several other years with FrIAC-like signatures: 1982, 1994, 1997, 2000, 2002, and 2004. That the number of FrIAC-like events is increasing (one during 1980–1989, two during 1990–1999, and five during 2000–2009) suggests there may be an increasing probability of FrIAC events. According to Allen *et al.* [2012], the 2011 FrIAC had by far the lowest TrEL values and the strongest easterly vortex of any year from 1979 to 2011. This large-scale FrIAC also resulted in NO<sub>2</sub> columns above Eureka, Canada that were approximately twice as large as in previous years [Adams *et al.*, 2013]. Ozone within the FrIAC became depleted due to NO<sub>x</sub> reactions, with April-to-May loss that was greater than any other year studied (2004–2010).

[5] The first goal of this paper is to provide a comprehensive overview of the dynamical development and the transport and mixing processes associated with the 2011 FrIAC. In addition to examining the synoptic development of the feature, we introduce a diagnostic tool to isolate FrIAC air from its surroundings. This involves determination of the anticyclone edge using the *Q* diagnostic, which is a measure of the relative contribution of strain and rotation on the horizontal wind field [Haynes, 1990]. This edge determination allows calculation of a number of dynamical and chemical properties of the 2011 FrIAC and provides a framework for future quantitative comparison of different FrIAC events. The second goal of this paper is to test the ability of two different models (both a 3-D chemistry and transport model (CTM) as well as a high-resolution 2-D (latitude × longitude) isentropic transport model), driven by a particular meteorological analysis, to simulate such an event. The complex relations of the dynamics, large-scale transport, and chemistry involved in the Arctic spring-to-summer transition make this a very challenging period to observe and simulate.

[6] The paper is outlined as follows. In section 2, we describe the meteorological analyses and satellite tracer observations used in this study, and in section 3, we describe

3-D and 2-D (latitude × longitude) models used to simulate tracer transport in the FrIAC. In section 4, we detail the dynamical evolution of the FrIAC, while section 5 focuses on the evolution of the long-lived tracer nitrous oxide (N<sub>2</sub>O) within the FrIAC by comparing satellite observations with model simulations. Sections 6 and 7 provide a summary and discussion, respectively.

## 2. Data and Analysis Description

### 2.1. MLS Data

[7] The Aura Microwave Limb Sounder (MLS) measures millimeter-wavelength and submillimeter-wavelength thermal emission from the limb of Earth's atmosphere [Waters *et al.*, 2006]. The Aura MLS points in the direction of orbital motion and vertically scans the limb in the orbit plane, leading to data coverage from 82°S to 82°N latitude on every orbit. Profiles are measured every 165 km (~1.5° great circle) along the suborbital track. We use version 3.3 N<sub>2</sub>O, which is generally similar to version 2.2 N<sub>2</sub>O, which was validated in Lambert *et al.* [2007]. Additional details on version 3.3 data quality are provided in Livesey *et al.* [2011]. Vertical resolution of the N<sub>2</sub>O data is ~4–6 km for the region of interest in this study (approximately 30–1 hPa). Horizontal resolution is ~300–600 km along-track, while the cross-track resolution is set by the 3 km width of the MLS 640-GHz field-of-view. In the 46–1 hPa range, the single profile precision is ~13–16 ppbv and the estimated accuracy decreases monotonically with altitude from 32 to 0.6 ppbv. In percentage terms, the accuracy is ~9–14% in this pressure range, while the precision increases monotonically with altitude from 7% at 46 hPa to greater than 100% at 2 hPa where the N<sub>2</sub>O mixing ratio is small. The N<sub>2</sub>O data are screened using the quality control criteria in Livesey *et al.* [2011] and are vertically interpolated from the retrieved pressure levels to potential temperature, which is calculated from the MLS temperature profiles. The version 3.3 MLS temperature is similar to the version 2.2 product described in Schwartz *et al.* [2008]. It has a precision of 1 K or better from 316 to 3.16 hPa and a pressure-dependent bias between –2.5 and +1 K between 316 and 10 hPa [Livesey *et al.*, 2011].

### 2.2. Meteorological Data

[8] The dynamical fields used in this study are from the Modern Era Retrospective Analysis for Research and Applications (MERRA) reanalysis. The MERRA reanalysis extends from 1979 to the present and uses the GEOS-5 data assimilation system (version 5.20) throughout, providing a consistent analysis that includes online bias correction for satellite radiance observations [Rienecker *et al.*, 2011]. To document the FrIAC dynamics, we use the 6-hourly instantaneous analyzed state on 42 pressure levels (top at 0.01 hPa) with horizontal resolution of 0.50° latitude × 0.67° longitude (selected data product: *inst6\_3d\_ana\_Np*). PV and streamfunction are calculated once daily (at 12 Z) from the MERRA winds and temperatures at the 13 isentropic surfaces used in this study (460, 520, 580, 650, 740, 850, 960, 1100, 1300, 1450, 1700, 1900, and 2100 K). PV is converted to equivalent latitude (EL) units, termed PVEL to distinguish from TrEL, described in section 3.2. The MERRA fields (at different spatial and temporal resolutions) are also used to drive both models described in section 3, so the diagnostics are dynamically consistent with the models.

### 2.3. Anticyclone Edge Diagnostic

[9] In this study, we examine the evolution of the 2011 FrIAC using an algorithm to determine the anticyclone edge, thereby isolating the air within the anticyclone from ambient air. The anticyclone edge is determined using the “ $Q$  diagnostic” approach discussed in *Harvey et al.* [2002]. This approach is based on the scalar quantity  $Q$  (defined below), which is a measure of the relative contribution of strain and rotation on the wind field [see also *Haynes*, 1990; *Fairlie*, 1995; *Fairlie et al.*, 1999].

$$\begin{aligned} Q = & \frac{1}{2} \left( \frac{1}{a \cos \varphi} \frac{du}{d\lambda} - \frac{v}{a} \tan \varphi \right)^2 + \frac{1}{2} \left( \frac{1}{a d\varphi} \frac{dv}{d\lambda} \right)^2 \\ & + \left( \frac{1}{a^2 \cos \varphi} \frac{du}{d\varphi} \frac{dv}{d\lambda} + \frac{u \tan \varphi}{a^2} \frac{du}{d\varphi} \right) \end{aligned}$$

[10] Here,  $u$  and  $v$  are the zonal and meridional wind components,  $\lambda$  and  $\varphi$  are the longitude and latitude, and  $a$  is the Earth’s radius.  $Q$  is positive (negative) where strain (rotation) dominates the flow. Inside coherent vortices, the rotational flow dominates, while outside the vortices strain becomes significant. Integrating  $Q$  around streamlines can therefore provide an objective determination of the anticyclone edge as the streamline in which the line integral of  $Q$  changes sign. This technique has been successfully applied to analyses of anticyclones in the winter and spring [*Harvey et al.*, 2002, 2004, 2008]. Here, we apply this approach to isolate air within the developing large-scale FrIAC and the subsequent evolution of the summer vortex. The algorithm we use calculates the line integral for streamfunction values at an interval of  $0.5 \times 10^7 \text{ m}^2/\text{s}$ . In order to restrict the line integral to closed streamlines, we had to constrain the latitude range over which the integral was calculated. Up to 3 April, we used the entire Northern Hemisphere (NH), while after 3 April, we limited the calculation to  $40\text{--}90^\circ\text{N}$ . These criteria are sufficient for isolating the 2011 FrIAC event. For different scenarios, particularly in the presence of multiple anticyclones, more complicated algorithms may be required [e.g., *Harvey et al.*, 2002].

## 3. Models

### 3.1. Global Modeling Initiative Chemistry and Transport Model

[11] Results are presented from the Global Modeling Initiative (GMI) CTM, hereafter GMI, driven by MERRA fields at  $1.00^\circ$  latitude  $\times$   $1.25^\circ$  longitude horizontal resolution and 72 vertical levels (model top of 0.01 hPa). The vertical resolution in the region of interest for this study (approximately 30–1 hPa) is  $\sim 1.1\text{--}1.5 \text{ km}$ . The GMI advection core uses a modified version of the flux form semi-Lagrangian numerical transport scheme [*Lin and Rood*, 1996]. The GMI is an offline computation that reads meteorological fields, including temperatures, winds, and subgrid transport quantities (e.g., convective transport) from the MERRA analyses, which are updated every 6 h. The vertical winds are calculated from the analyzed horizontal winds using divergence and the continuity constraint. The GMI chemistry combines the stratospheric chemistry described in *Douglass et al.* [2004] with tropospheric chemistry from the Harvard GEOS-Chem model

[*Bey et al.*, 2001], as discussed in *Strahan et al.* [2007]. Transport diagnostics based on observed  $\text{N}_2\text{O}$  and mean age [*Strahan et al.*, 2011] show that the GMI with MERRA meteorological fields have very good representations of lower stratospheric tropical ascent and horizontal mixing.

### 3.2. Van Leer Icosahedral Triangular Advection Model

[12] This study also uses the Van Leer Icosahedral Triangular Advection (VITA) model driven by MERRA winds in order to calculate TrEL, which has been previously used to produce realistic tracer fields for studies of stratospheric transport and mixing including calculation of effective diffusivity, reconstruction of ozone miniholes, analysis of aircraft campaign data in the polar lower stratosphere, examination of transport during the 2002 Antarctic major warming, and as a diagnostic for determining FrIAC occurrence [*Allen and Nakamura*, 2001, 2002, 2003; *Allen et al.*, 2003, 2012]. A complete description of the VITA model is provided in *Allen and Nakamura* [2003] along with modifications discussed in *Allen et al.* [2011]. Briefly, VITA uses an Eulerian finite-volume advection scheme on an icosahedral triangular grid with a van Leer flux limiter. For the TrEL calculation, a tracer is initialized on 1 January 1979 (12 Z) with mixing ratio equal to the sine of latitude, and 20,480 triangles (resolution  $\sim 240 \text{ km}$ ) are used. The TrEL simulation runs through 2011, providing a continuous 33-year time series, although only the final year is used in this study. The tracer mixing ratio is normalized each time step to global minimum/maximum values of  $-1/+1$  using a simple linear operator. The tracer mixing ratio is saved once per day (12 Z) and TrEL is calculated using  $\text{TrEL}(q) = \sin^{-1}(A(q)/2\pi a^2 - 1)$ , where  $A(q)$  is the area with mixing ratio  $q$  less than a given value and  $a$  is the Earth’s radius. Since the tracer is global, TrEL ranges from  $-90^\circ$  to  $+90^\circ$ . Since TrEL scales like latitude, it is useful for highlighting latitudinal transport. For example, low-TrEL values at the North Pole indicate poleward transport and high-TrEL values in the tropics indicate equatorward transport. TrEL simulations are forced by the isentropic streamfunction (derived from MERRA fields, see section 2.2) at 24-h intervals interpolated linearly in time to the model time step (8 min) and linearly in space to the model grid.

[13] The VITA model is also used for high-resolution simulations of isentropic  $\text{N}_2\text{O}$  transport, in order to compare with GMI and MLS  $\text{N}_2\text{O}$ . These simulations are performed with 983,040 triangles (resolution  $\sim 20 \text{ km}$ ) and are initialized with gridded MLS  $\text{N}_2\text{O}$  maps, which are made using spatially weighted averages of each day’s data in the region around each gridpoint on a  $2.0^\circ$  latitude  $\times$   $5.0^\circ$  longitude grid. Data values in the region not observed by MLS (poleward of  $82^\circ\text{N}$ ) are calculated by interpolating over the polar region from neighboring grids. MERRA horizontal winds at 24-h intervals are interpolated vertically to isentropic surfaces, linearly in space to the model grid, and linearly in time to the model time step (30 s) in order to drive the high-resolution VITA simulations.

## 4. Dynamical Evolution of the 2011 Large-Scale FrIAC

[14] The 2011 Arctic winter vortex experienced more chemical ozone loss than any other previous year [*Manney*

*et al.*, 2011] due to unusually cold temperatures in the polar lower stratosphere in late February and March, associated with weak planetary wave driving [Hurwitz *et al.*, 2011]. As discussed in Allen *et al.* [2012], the 2011 vortex experienced an abrupt SFW due to rapid anticyclone development classified as a large-scale FrIAC. In this section, we document the dynamics of this event by examining the evolution of zonal wind, PVEL, TrEL, and streamfunction and also determine the boundary of the FrIAC using vortex edge diagnostics, which is used for examining various FrIAC properties.

#### 4.1. Dynamical Evolution Using Zonal Wind, PVEL, and TrEL

[15] Figure 1a shows the zonal mean zonal wind at 850 K potential temperature ( $\sim 32$  km) from March to August 2011. The edge of the winter polar vortex is located at  $\sim 70^\circ\text{N}$  in March with a westerly zonal wind speed of  $\sim 60$  m/s. In late March, the vortex experiences an initial deceleration to  $\sim 20$  m/s, which is caused by anticyclonic development over North America (more details below). The second deceleration, the SFW, occurs in early April, resulting in wind reversal to easterly values of  $\sim 30$  m/s around 10 April. This dramatic SFW was documented in Allen *et al.* [2012] as achieving the strongest easterly winds following any SFW during the 33-year period from 1979 to 2011; this condition favors poleward motion and trapping of low-latitude air into

the summer vortex. The easterlies cover a broad latitude range from  $\sim 45^\circ\text{N}$  to the pole, while westerlies remain in the subtropics until mid-May, after which winds are easterly over the entire NH. The strength of the polar easterly vortex decelerates over the next several months, reaching a steady easterly value of  $\sim 10$  m/s in June and early July. The final reversal back to winter westerlies at  $70^\circ\text{N}$  occurs in late August. Note that the quasi-biennial oscillation is in the easterly phase during this SFW and there were no major warmings previous to the SFW, both conditions that favor FrIAC formation [Thiéblemont *et al.*, 2011]. Figure 1b shows the zonal wind at  $75^\circ\text{N}$  over the vertical range from 460 to 1900 K ( $\sim 20$ – $50$  km). The zonal wind evolution at all levels is qualitatively similar to that at 850 K, with a strong winter jet reversing rapidly to easterlies in early April and reversing back to westerlies in late August. We will examine the vertical wind structure further in section 5.1.

[16] Figure 2 shows NH maps for select days in March and April 2011 at 850 K. The top two rows include PVEL, streamfunction, and edge identification, while the bottom two rows include TrEL with edge identification. On 27 March, the polar vortex, indicated by high PVEL, is located off the pole due to a short-lived anticyclone over North America (indicated by a closed streamline centered over Canada, marked with low PVEL). From 27 March to 1 April, the North American anticyclone first strengthens (as indicated by multiple streamlines on 29 March) and then weakens, disappearing by 7 April. On 27 March, the second anticyclone, highlighted with a red edge contour, exists over Northern Africa. This is the anticyclonic “seed” of what will eventually be the large-scale FrIAC (we will hereafter call this feature “the FrIAC” or “the anticyclone” interchangeably). From 29 March to 1 April, the FrIAC begins to move eastward and poleward and increases in strength (later we will quantify the strength of the FrIAC in terms of flow around the vortex edge). By 4 April, the FrIAC has traveled nearly halfway around the globe, bringing with it low PVEL air from the subtropics. From 4 to 10 April, the FrIAC continues to move poleward, displacing the winter vortex, which elongates and stretches completely around the FrIAC (see high PVEL values forming a ring around the FrIAC on 7 and 10 April). By 10 April, the FrIAC is establishing its position at the pole and is characterized by low PVEL values throughout. The edge of the FrIAC on 10 April just crosses the pole. For this year, one could define the date of the SFW, rather than using the zonal mean wind reversal, which has ambiguities due to choice of threshold wind, latitude range, and time smoothing [e.g., Wei *et al.*, 2007]. For comparison, Allen *et al.* [2012] calculated an SFW date of 6 April 2011 using the 10 hPa,  $60$ – $70^\circ\text{N}$  average MERRA zonal winds, smoothed with a 5-day running mean and with a threshold of zero.

[17] The combination of multiple anticyclones leading to FrIAC development was also observed in the 2005 FrIAC episode [Allen *et al.*, 2011]. Similarly, in 2005, an Aleutian High caused initial displacement of the winter polar vortex, followed several days later by a traveling anticyclone, which originated in Africa and moved eastward and poleward, completely displacing the winter polar vortex. One difference in 2005 was the presence of stationary high over Tibet, which merged with the traveling anticyclone before the final FrIAC development. Another difference was that in 2005,

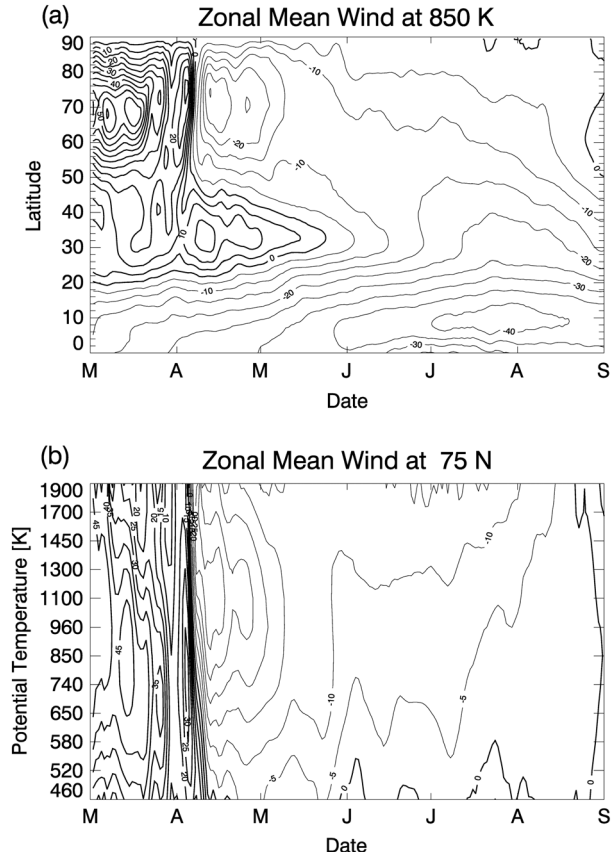


**Figure 1.** (a) NH zonal mean zonal wind at 850 K ( $\sim 32$  km) potential temperature for March–August 2011. (b) Zonal mean zonal wind at  $75^\circ\text{N}$  from 460 to 1900 K ( $\sim 20$ – $50$  km) for March–August 2011. Thick (thin) lines indicate eastward (westward) winds.

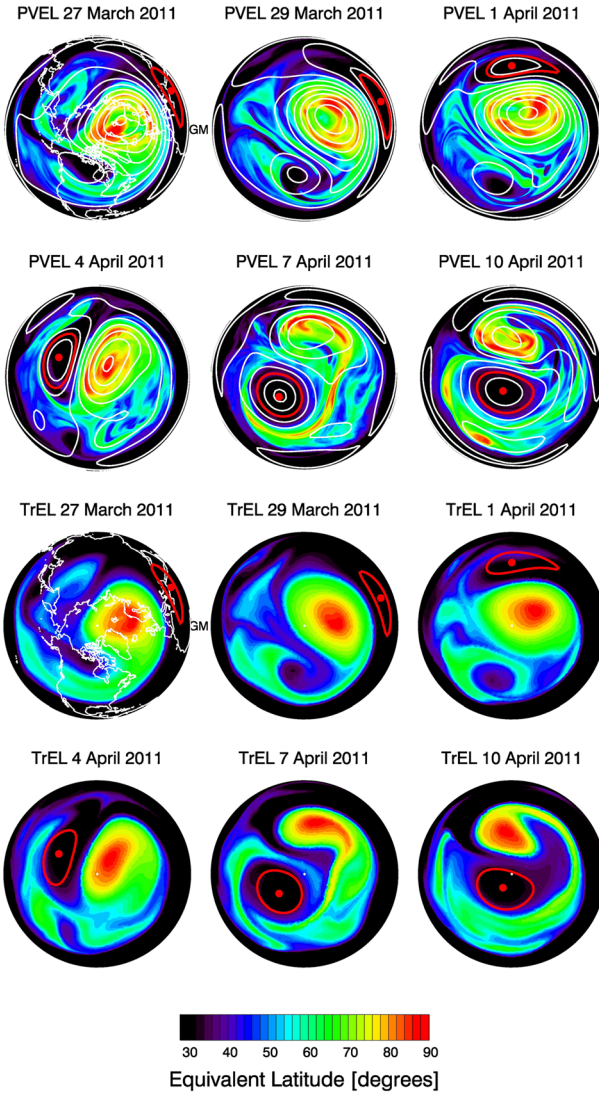


**Figure 2.** Rows 1 and 2: NH PVEL at 850 K ( $\sim 32$  km) for select days from 27 March to 10 April 2011. Maps are orthographic projection with Greenwich Meridian to the right. White lines show streamfunction at regular intervals of  $2 \times 10^7 \text{ m}^2/\text{s}$ . Red line indicates the edge of the anticyclone and red circle indicates the anticyclone center (see text for details). Rows 3 and 4: NH TrEL at 850 K for select days from 27 March to 10 April 2011, with anticyclone edge highlighted with red line. In all plots, red/blue contours indicate high/low equivalent latitude.

the FrIAC became embedded into the developing easterly flow and circulated around the pole, rather than being immediately established at the pole, as in 2011. The occurrence of multiple anticyclones may indicate that a preconditioning of the vortex is necessary for FrIAC development. In 2011, for example, the anticyclone over North America weakened the vortex and pushed it off the pole. This led to strong poleward motion off the eastern flank of the vortex, which facilitated anticyclonic spin-up due to conservation of PV. Preconditioning of the polar vortex has been discussed for stratospheric sudden warmings [e.g., *Bancala et al.*, 2012, and references therein] but not (as far as we are aware) in the context of the SFW.

[18] The TrEL maps look qualitatively similar to the PVEL maps for this period. Low-TrEL air accompanies the traveling anticyclone as it moves eastward and poleward and becomes established near the pole. High-TrEL air traces out the winter polar vortex evolution as it is stretched around the developing FrIAC. The TrEL field is considerably smoother than the PVEL. This is due to a combination of factors. First, while TrEL and PVEL are both derived from the same meteorological analyses, TrEL is calculated at lower resolution ( $\sim 240$  km triangular grid) than PVEL ( $0.50^\circ$  latitude  $\times 0.67^\circ$  longitude, which is approximately  $50$  km  $\times 75$  km at the equator). Second, TrEL is a time-integrated quantity that involves implicit numerical mixing, whereas PVEL is calculated from the instantaneous wind and temperature fields. TrEL therefore has an advantage in that some of the small-scale noise in the analyzed fields is smoothed out during the time integration. Third, TrEL is a passively defined tracer, whereas PVEL has sources due to diabatic heating/cooling. The differences between the two fields in Figure 2 are due primarily to the first and second factors, while diabatic processes are more important in the upper stratosphere as well as in the middle and lower stratosphere later in the spring and summer (see *Allen and Nakamura* [2003] for more detailed comparisons of TrEL and PVEL).

[19] To determine the initial vertical structure of the 2011 FrIAC, in Figure 3, we show PVEL and TrEL at multiple isentropic levels for 8 April 2011. Closed streamlines with a well-defined edge extend from 580 K ( $\sim 25$  km) to 2100 K ( $\sim 50$  km), indicating a vertical range of  $\sim 25$  km. This structure extends higher than the 2005 FrIAC, which was observed from 580–1100 K ( $\sim 25$ –40 km) [Allen et al., 2011]. Low TrEL dominates the area within the anticyclone over the entire 580–2100 K range, while at 1700 K and above, low PVEL covers only part of the anticyclone (the 1700 K PVEL plot, not shown, is similar to the 1900 K PVEL plot). This is likely due to diabatic processes in the upper stratosphere, which prevent PV from acting like a passive tracer. The FrIAC shows a rather strong tilt with the center tipping towards the pole with increased altitude. Whereas at 580 K, the anticyclone is centered off the western coast of North America, at 2100 K, it extends beyond the pole into the eastern hemisphere. As the FrIAC becomes established over the pole, the vertical tilt is greatly reduced. By 20 April (not shown), for example, the FrIAC is pole centered with almost no tilt from 580 to 2100 K. In the summer stratosphere, when wave activity weakens, the polar region is dominated by diabatic processes that tend to maintain a strong zonal flow.

[20] The decay of the dynamical signature of the FrIAC is examined in Figure 4, which shows maps of PVEL and TrEL for select days in May and June 2011. On 1 May, low PVEL and low TrEL fill the summer vortex (edge identified with red contour). Over the next several weeks, the low PVEL region shrinks steadily so that by 25 May, it is a confined to a very small circular area near the pole. This low PVEL feature circulates in an easterly direction (clockwise) around the pole for several weeks, slowly decreasing in size with time, but remaining as a coherent feature until at least mid-June. The remnant of the PVEL anomaly on 18 June is seen as a thin tube over western Canada, and by 26 June, the low PVEL signature has disappeared completely. By this time, high PVEL values encompass the polar region. The

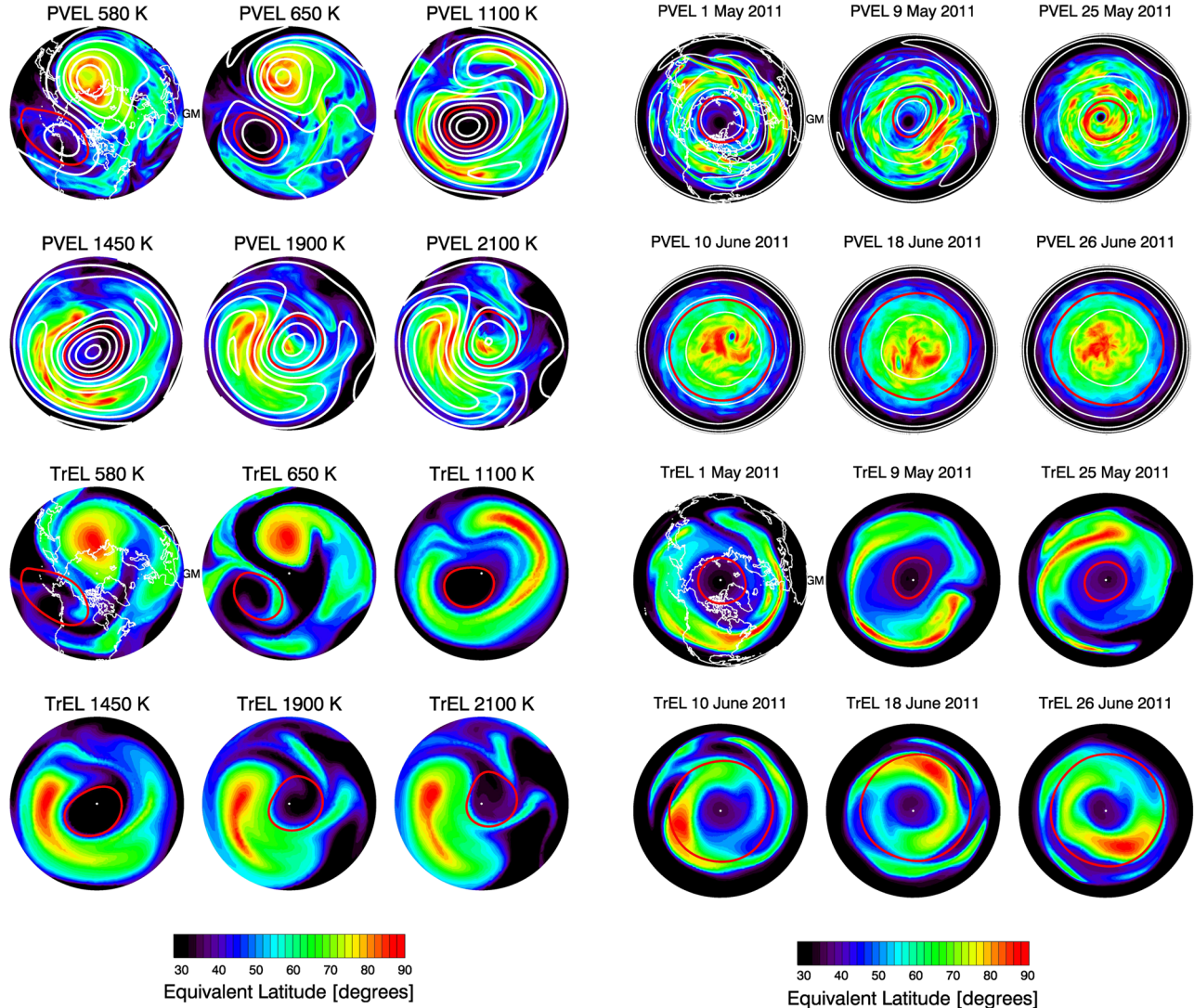


**Figure 3.** Rows 1 and 2: PVEL from 30 to 90°N at multiple isentropic levels from 580 to 2100 K (~25–50 km) for 8 April 2011. White lines show streamfunction at regular intervals of  $2 \times 10^7 \text{ m}^2/\text{s}$ . Red lines indicate the edge of the anticyclone. Rows 3 and 4: TrEL from 30 to 90°N over the same range of isentropic levels for 8 April 2011, with anticyclone edge highlighted with red line. In all plots, red/blue contours indicate high/low equivalent latitude.

TrEL field, in contrast to PVEL, remains steadily low throughout the vortex in May, with only a slight increase of the mean value with time. Around 2 June (not shown), the edge of the anticyclone, as determined by the  $Q$  diagnostic, expands outwards as the zonal easterly circulation begins to encompass the entire NH (see also Figure 1a). This indicates that the FrIAC is no longer an independent entity within the summer easterly regime but has been encompassed by the developing summer vortex (this marks the shift from the “anticyclonic phase” to the “shearing phase”). A region of high-TrEL air is visible throughout this period, forming a nearly complete ring around the summer polar vortex. High-TrEL indicates air that originated in the winter polar vortex but became wrapped around the developing anticyclone. Much of this high-TrEL air is

**Figure 4.** Rows 1 and 2: NH PVEL at 850 K (~32 km) for select days from 1 May to 26 June 2011. White lines show streamfunction at regular intervals of  $2 \times 10^7 \text{ m}^2/\text{s}$ . Red lines indicate the edge of the anticyclone. Rows 3 and 4: NH TrEL at 850 K for select days from 1 May to 26 June 2011, with anticyclone edge highlighted with red line. In all plots, red/blue contours indicate high/low equivalent latitude.

encompassed into the summer vortex as it grows in size by the end of June.

#### 4.2. Dynamical Evolution Using Vortex Edge Diagnostics

[21] The synoptic maps in section 4.1 provide a qualitative view of the evolution of the 2011 FrIAC. In Figure 5, this process is quantified using a number of diagnostics related to FrIAC location, size, strength, and composition of PVEL and TrEL, from its initial identification on 27 March through 26 May, 60 days later. In Figure 5a, the location is given in terms of the latitude and longitude of the maximum streamfunction value within the FrIAC (identified with a red dot in Figure 2). The poleward and eastward motion in early April is seen as the FrIAC moves from 30 to 80°N

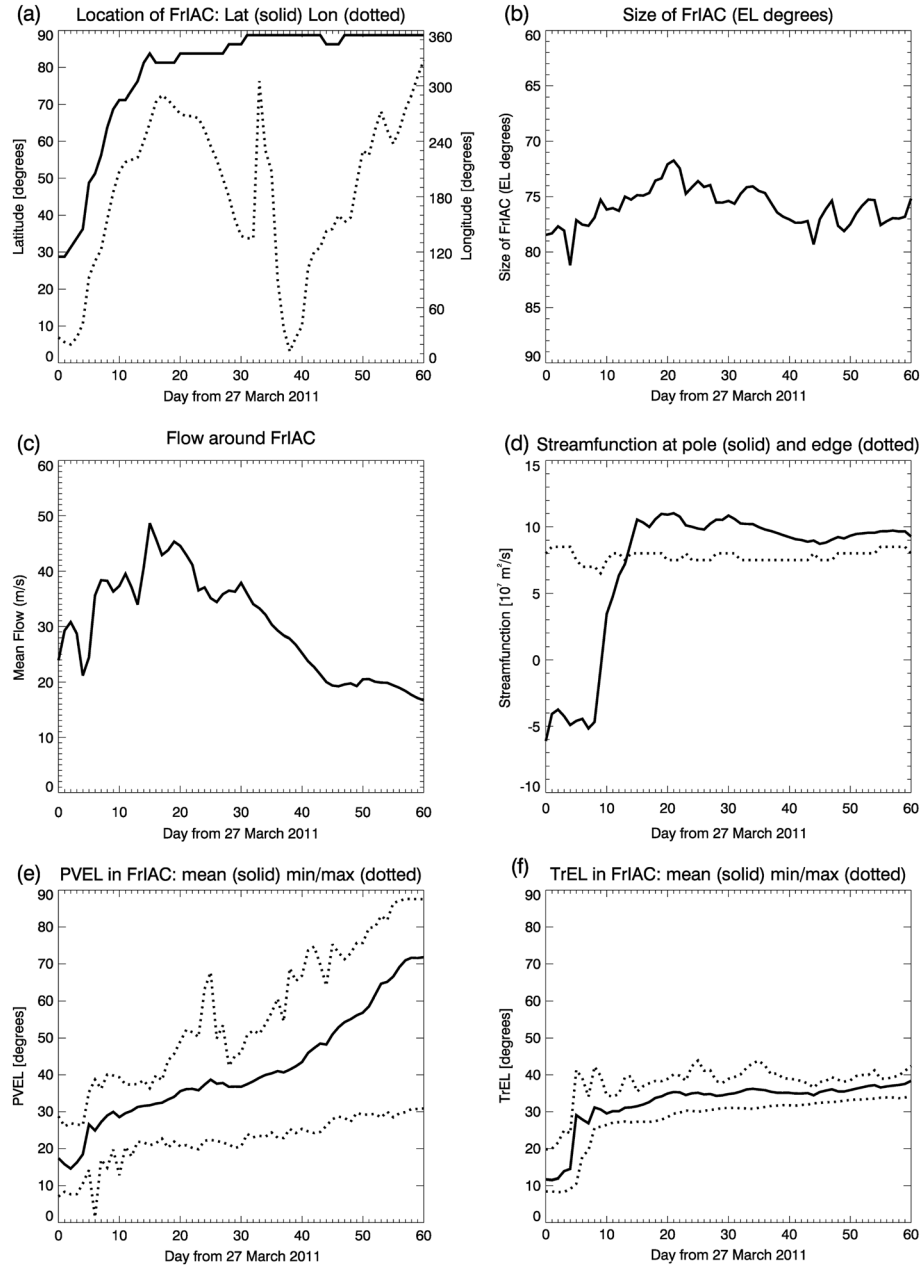


**Figure 5.** Diagnostics related to the FrIAC evolution at 850 K (~32 km) from 27 March to 26 May 2011: (a) location: latitude (solid line), longitude (dotted line), (b) size in equivalent latitude (EL) units, (c) flow around the edge, (d) streamfunction at the pole (solid line) and edge (dotted line), (e) mean (solid line) and minimum and maximum (dotted lines) values of PVEL, and (f) mean (solid line) and minimum and maximum (dotted lines) values of TrEL.

and from 30 to 270°E over the course of about 2 weeks. The FrIAC remains at high latitudes for the rest of the period, established as the core of the summer easterly vortex, while the longitude varies as the center of the FrIAC meanders about the pole (note that when the anticyclone is over the pole, large changes in longitude do not correspond to large changes in the location of the center of the anticyclone). The size of the FrIAC is provided in Figure 5b in terms of the area enclosed by the edge contour. This area is converted to EL units, so that lower EL indicates larger size. The FrIAC increases in size over the first 20 days, reaching a minimum EL of  $\sim 72^\circ$ , and then slowly decreases in size.

The high-frequency noise in the size is likely due to uncertainties in the  $Q$  calculation that are reflected in slight variations in the edge value. The flow around the FrIAC is determined by averaging the wind speed along the FrIAC edge (Figure 5c). The flow increases from  $\sim 25$  to  $\sim 50$  m/s as the FrIAC moves poleward. The increase in flow is not monotonic but has several maxima and minima, again likely due to noise in the  $Q$  calculation. The general increase in flow is consistent with the process of PV conservation; as the planetary vorticity increases, the relative vorticity (related to the flow) will decrease. Since the anticyclone has a negative relative vorticity, the magnitude will increase,

therefore causing an increase in the flow. Figure 5d shows the streamfunction value at the edge of the anticyclone (dotted) and at the pole (solid). Whereas the polar value increases sharply from  $-5 \times 10^7$  to  $+10 \times 10^7 \text{ m}^2/\text{s}$ , the edge value remains fairly constant throughout the time period. As seen in Figure 2, the edge crosses over the pole on 10 April (day 14 in Figure 5d) and encompasses the pole throughout the rest of the period.

[22] While Figure 2 shows low PVEL and TrEL values within the FrIAC, a more quantitative view is helpful to understand the evolution of the air mass within the FrIAC. We therefore examined all of the PVEL and TrEL values for model grid points that were located within the FrIAC edge. The minimum, maximum, and area-weighted mean values are plotted in Figures 5e (PVEL) and 5f (TrEL). Both PVEL and TrEL show very low mean values (less than  $20^\circ$ ) at the beginning of the time period. As the FrIAC starts to move poleward over the first 5 days, the mean values jump to  $\sim 30^\circ$ , suggesting that air encompassed by the FrIAC on 27 March does not remain within the FrIAC but is replaced by higher latitude air. From day 5 (1 April) onward, however, the mean TrEL and PVEL values level out considerably, suggesting that the air enclosed by the FrIAC remains relatively unmixed with air outside the FrIAC. The minimum and maximum TrEL values also remain relatively constant over this period, with a narrow range of  $\sim 10^\circ$ . Further proof of the isolation of air inside the FrIAC will be examined in more detail in section 5 using observations and simulations of N<sub>2</sub>O. The PVEL has a larger range of values ( $\sim 20^\circ$ ) than TrEL after the initial formation, and the mean PVEL increases slowly over the first month. During the second month (days 30–60), the mean PVEL doubles from  $35^\circ$  to  $70^\circ$ . This is due to diabatic effects that tend to eliminate the low PVEL signature with time. While the maximum PVEL increases sharply, the minimum PVEL remains quite low, reaching only  $\sim 30^\circ$  by day 60. This is due to the small PVEL feature that persisted within the anticyclone (Figure 4). The TrEL mean value and range remain small throughout this period, suggesting that long-lived tracers will maintain relatively constant values within the FrIAC. In the next section, we will examine this in more detail using observations and simulations of the long-lived tracer N<sub>2</sub>O.

## 5. Tracer Transport During the 2011 Large-Scale FrIAC

[23] The evolution of PVEL and TrEL discussed in section 4 implies that the signature of the FrIAC should also be seen in long-lived tracers. Several previous studies have examined the FrIAC lifecycle using satellite observations of H<sub>2</sub>O, CH<sub>4</sub>, and N<sub>2</sub>O data [Manney et al., 2006; Lahoz et al., 2007; Allen et al., 2011; Thiéblemont et al., 2011]. Here, we use MLS N<sub>2</sub>O data along with GMI and VITA simulations to examine the 2011 FrIAC. An instrument anomaly prevented MLS from making measurements from 27 March to 19 April 2011. In lieu of observations, global 2-D and 3-D N<sub>2</sub>O simulations will be used for this period, while MLS data will be used to validate the later stages of the FrIAC.

### 5.1. Tracer Transport Using Observations and Model Simulations of N<sub>2</sub>O

[24] Figure 6 shows GMI N<sub>2</sub>O at 850 K for the same days as in Figure 2. On 27 March, low N<sub>2</sub>O values occur

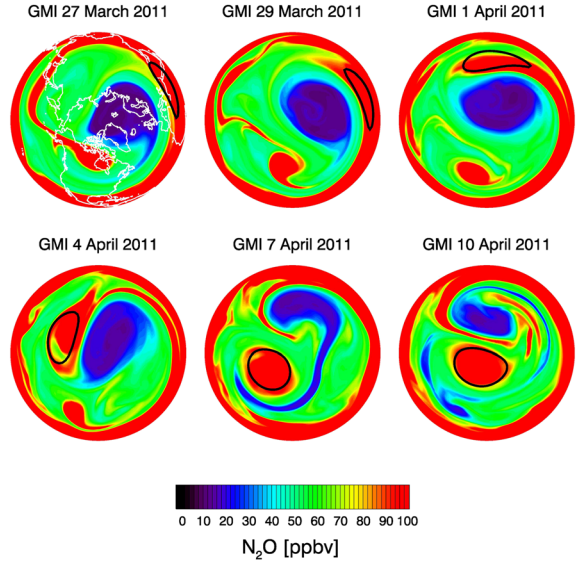


**Figure 6.** NH GMI N<sub>2</sub>O at 850 K ( $\sim 32$  km) for select days from 27 March to 10 April 2011. The anticyclone edge is indicated by the black line. In all plots, red/blue contours indicate high/low N<sub>2</sub>O.

throughout the winter polar vortex, while high values exist in the tropics and in a long tongue of air stretching across the North Pacific and Canada. Early developments of this tongue were observed in MLS N<sub>2</sub>O on 25 March (not shown) before the instrument shut down. The high N<sub>2</sub>O at the tip of this tongue spins up into the North American anticyclone on 29 March–1 April but later disperses as this anticyclone decays. The FrIAC development over Africa shows high N<sub>2</sub>O accompanying the traveling anticyclone as it moves eastward and poleward from 29 March to 10 April. On 4 April, the N<sub>2</sub>O is not uniformly high in the FrIAC, since a region of lower N<sub>2</sub>O appears inside the edge. This lower N<sub>2</sub>O mixes with ambient air over the next few days, however, leaving fairly uniform N<sub>2</sub>O in the FrIAC (examined later in time-series plots of the minimum and maximum N<sub>2</sub>O values). The low N<sub>2</sub>O that originated in the winter polar vortex is stretched out into a thin ribbon around the FrIAC on 7 April, similar to what was observed in PVEL and TrEL (Figure 2). There is a complicated mixture of high and low N<sub>2</sub>O structures in the extratropics on 10 April, as generally occurs following the SFW [Hess, 1991; Orsolini, 2001].

[25] Validation of the GMI results with MLS data during the formation of the 2011 FrIAC was not possible due to the instrument anomaly. The instrument started again on 19 April, with the first full day of measurements available on 20 April. From 10 to 20 April, the FrIAC at 850 K remained relatively undiminished in size and centered close to the pole, while the low N<sub>2</sub>O air associated with the winter polar vortex stretched out into thin filaments and mixed into the extratropics. In Figure 7, we examine GMI and MLS N<sub>2</sub>O on 21 April along two Aura orbit tracks that crossed through the FrIAC. We also include, for comparison, high-resolution ( $\sim 20$  km) VITA isentropic transport simulations that were initialized with gridded MLS N<sub>2</sub>O data on 25 March 2011. The synoptic maps of the GMI and VITA simulations (top row of Figure 7) show elevated N<sub>2</sub>O within the FrIAC, which is centered slightly off the pole towards

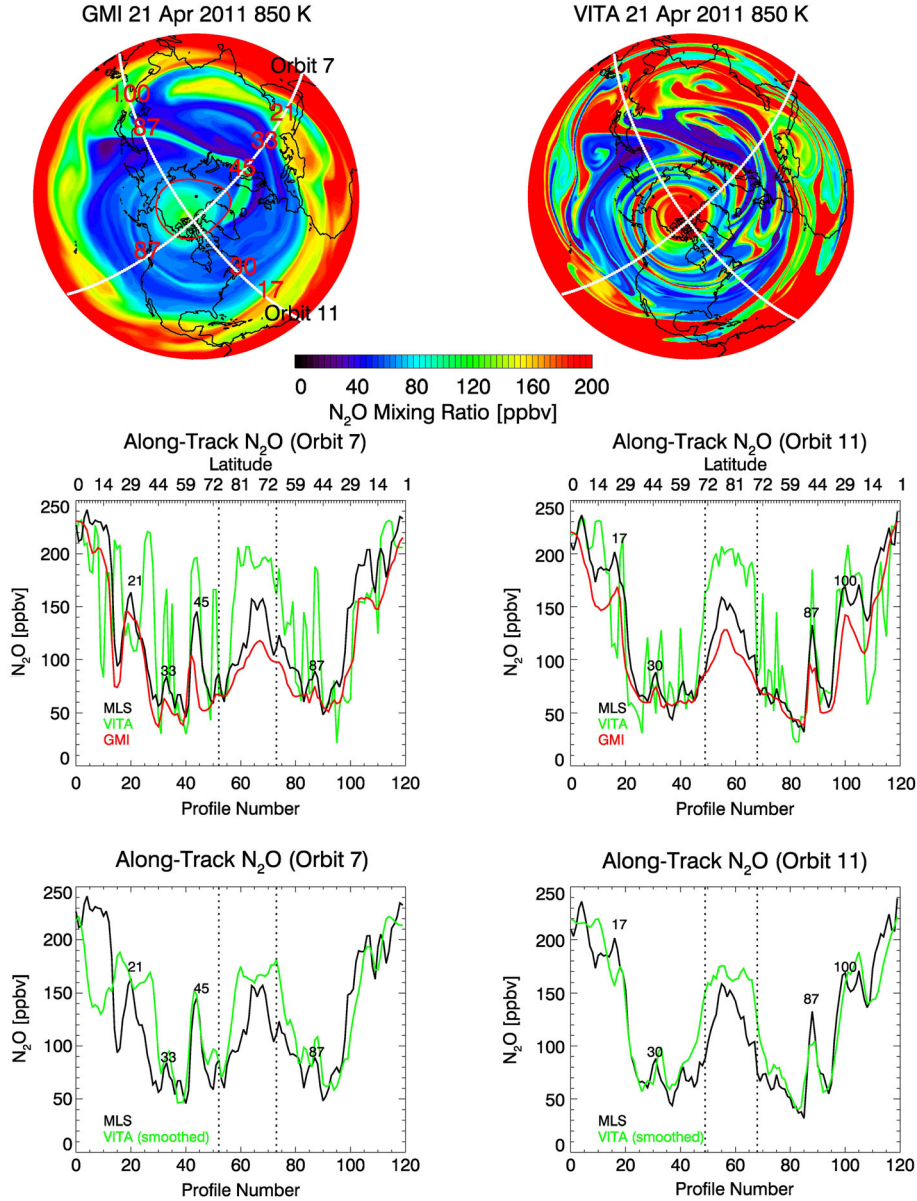


**Figure 7.** Top row: (left) NH GMI and (right) VITA  $\text{N}_2\text{O}$  at 850 K ( $\sim 32$  km) on 21 April 2011. Overlaid are two EOS Aura MLS orbit tracks for this day. In both plots, red/blue contours indicate high/low  $\text{N}_2\text{O}$ . Second row: (black) MLS, (red) GMI, and (green) VITA  $\text{N}_2\text{O}$  at 850 K along the selected MLS orbit tracks. The profiles start at the locations of the orbit labels in the upper left panel. GMI and VITA data are interpolated linearly in space and time to the MLS data points. The approximate latitude is provided on the top of the panels. Third row: same as second row, but with (black) MLS and (green) VITA data smoothed to resemble MLS vertical and horizontal resolution. See text for details.

North America. A tongue of high  $\text{N}_2\text{O}$  extends across northern Eurasia (see profile 45 in Orbit 7), while wisps of interwoven high and low  $\text{N}_2\text{O}$  filaments occur throughout the extratropics. The VITA simulation shows much more fine-scale structure than GMI. This is due both to the higher horizontal resolution of the VITA model and due to the neglect of vertical mixing in VITA, which is a 2-D (latitude  $\times$  longitude) isentropic simulation.

[26] Two along-track line plots of GMI, VITA, and MLS  $\text{N}_2\text{O}$  (second row of Figure 7) show considerable structure in the tracer field. In Orbit 7, there are at least seven distinct maxima. Tropical maxima occur at both the beginning

(profiles 0–10) and end (profiles 110–120) of the orbit track. Local maxima due to filamentary structure are observed centered near profiles 21, 33, 45, and 87 (also seen in the synoptic maps—profile numbers are labeled in red). The GMI simulation captures the shape of these structures; however, the peak amplitudes are underestimated. The VITA simulation captures most of these structures, although the filament near profile 21 in GMI is displaced to profile 26 in VITA. Also, the peak  $\text{N}_2\text{O}$  values in these filaments are generally higher in VITA than in MLS or GMI. The FrIAC, which occurs from profiles 52 to 73, shows maximum MLS  $\text{N}_2\text{O}$  values of  $\sim 150$  ppbv, which is larger than the maxima

in the GMI simulation. This is partly due to a low bias in the tropical N<sub>2</sub>O values in GMI (discussed further below). The VITA simulation apparently overestimates the N<sub>2</sub>O in the FrIAC with a peak at ~200 ppbv, compared to ~150 ppbv in MLS. As we show below, this can be largely explained by the vertical smoothing that occurs in the MLS retrieval. Orbit 11 crosses through filaments at profiles 17, 30, 87, and 100. The second filament (profile 30) is seen in the GMI map as a thin curved line of slightly elevated N<sub>2</sub>O extending over North America. The FrIAC occurs from profiles 49 to 68. Similar to Orbit 7, the GMI simulations underestimate the peak values within the FrIAC and are smoother than the MLS plots. The VITA simulation shows considerably more structure than GMI or MLS, as in Orbit 7, due to the much higher resolution, but all three are in qualitative agreement as to the overall N<sub>2</sub>O structure.

[27] There is variability in the MLS N<sub>2</sub>O within the FrIAC that is not well represented by GMI. The VITA simulation reveals N<sub>2</sub>O structure within the FrIAC that results in fluctuations on the same order as the MLS observations. The size of the fluctuations is on the order of the single profile precision at this level (~13 ppbv), so they are likely due to realistic tracer variability. That the VITA simulation has more structure in general than the MLS data may be partially explained by the MLS vertical resolution of ~4–6 km [Lambert et al., 2007], which smooths out vertically fine-scale features that may be well resolved in the 2-D model. To examine the smoothing effect, we performed two additional VITA simulations initialized with MLS data on 25 March but at potential temperature levels of 740 and 960 K, which span ~5 km in altitude. The resulting along-track N<sub>2</sub>O from these simulations were directly averaged along with the 850 K simulation to approximate the MLS

vertical resolution. To approximate the horizontal resolution of the MLS N<sub>2</sub>O data (~300–600 km), we applied a three-point smoothing (165 km along-track spacing  $\times$  3 = 495 km) to the along-track VITA data. The results are presented in the bottom row of Figure 7. The smoothed VITA data are in much better agreement with MLS than the unsmoothed data. The peak value within the FrIAC was reduced along with the peak values in several of the filaments, making the VITA simulated N<sub>2</sub>O much closer to that observed by MLS. The main differences are from profiles 0 to 30 along Orbit 7, in the tropics, where transport errors have accumulated to make larger errors in the VITA simulation. The otherwise good agreement with the smoothed VITA simulation and MLS data provides confidence that many of the fine-scale structures observed in the unsmoothed VITA simulation are realistic atmospheric features.

[28] As illustrated in Figure 7, there is a low bias of up to ~40–60 ppbv at 850 K in the GMI simulation of N<sub>2</sub>O in the FrIAC (a similar low bias was seen in GMI simulations of the 2005 FrIAC [Allen et al., 2011]). Since the FrIAC is composed of air transported from low latitudes, the simulated peak value will be dependent on the ambient N<sub>2</sub>O gradient preceding the FrIAC development. Figure 8 provides zonal mean plots of MLS and GMI N<sub>2</sub>O averaged over 1–15 March 2011. The MLS N<sub>2</sub>O plot shows high values due to ascent within the tropical pipe (0–20°N), a well-defined surf zone with weak horizontal gradients (20–60°N), and low N<sub>2</sub>O within the polar vortex (60–90°N). The GMI plot shows similar structures, although in the lower and middle stratosphere, the N<sub>2</sub>O values are generally smaller. Offline transport calculations using MERRA winds give mean age-of-air values that are somewhat high in the tropics, but MERRA tropical modal age (an indication of ascent rate)

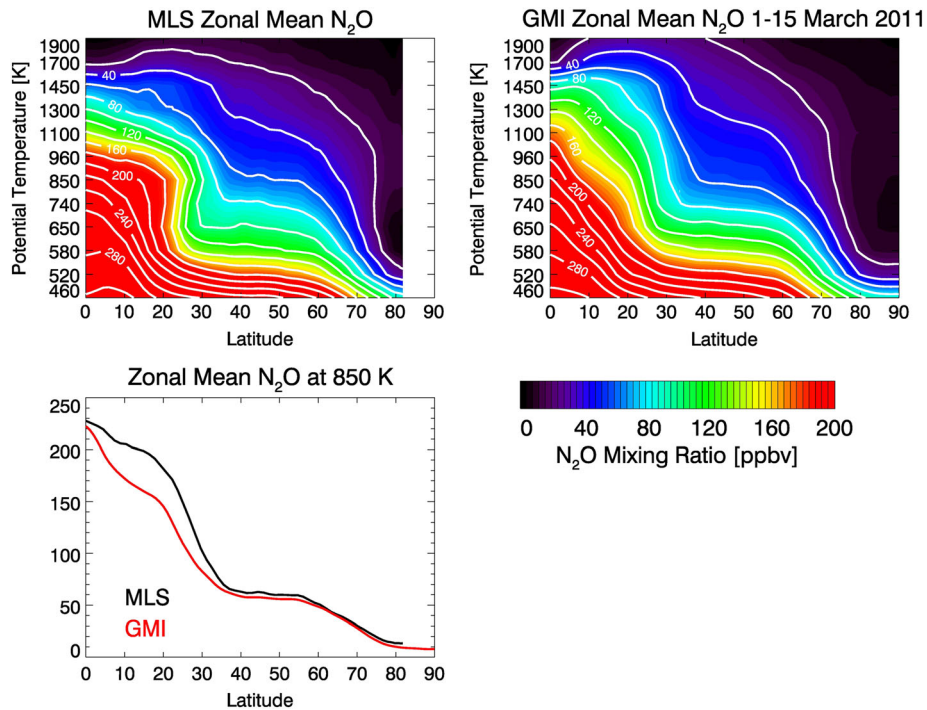


**Figure 8.** Zonal mean N<sub>2</sub>O cross-sections from (top left) MLS and (top right) GMI averaged over 1–15 March 2011. In both plots, red/blue contours indicate high/low N<sub>2</sub>O. (bottom left) Line plot is (black) MLS and (red) GMI zonal mean N<sub>2</sub>O at 850 K averaged over 1–15 March 2011.

agrees well with the ascent rate derived from the water vapor tape recorder [Schoeberl *et al.*, 2008]. Thus, the low tropical N<sub>2</sub>O in the GMI simulation is likely caused by subtropical mixing that is too strong (i.e., insufficiently isolated tropics). Line plots of N<sub>2</sub>O as a function of latitude at 850 K show biases in the subtropics of up to ~40 ppbv, which are consistent with the low bias in the GMI simulation of the FrIAC.

[29] Vertical cross-sections (“curtains”) of the MLS and GMI N<sub>2</sub>O fields along the orbit tracks shown in Figure 7 are provided in Figure 9. This view is similar to the pole-centered approach used by Lahoz *et al.* [2007] to examine the 2003 FrIAC with MIPAS CH<sub>4</sub> data. Elevated MLS N<sub>2</sub>O values are seen in the central regions of both orbits, with a peak anomaly observed at 740 K. The edge of the anticyclone is marked with white lines in Figure 9, showing almost no tilt of the FrIAC with height. The anomalous N<sub>2</sub>O extends from ~580 to 1700 K, although it becomes more difficult to identify in the upper stratosphere, where the N<sub>2</sub>O mixing ratios and spatial gradients become small and photochemical destruction become increasingly important.

The GMI simulation captures the general morphology of the MLS along-track curtains as well as some of the fine-scale features (e.g., the low N<sub>2</sub>O filaments near profiles 30 and 40 in Orbit 7 and near profile 90 in Orbit 11). The main weakness in the GMI simulation is an underestimation of the peak N<sub>2</sub>O mixing ratio in the center of the FrIAC, which as discussed above, is due to a low bias the subtropical GMI N<sub>2</sub>O values in the lower stratosphere, relative to MLS. Note, however, that MLS accuracy is ~32 ppbv (14%) in the lower stratosphere, so there may be observational biases as well.

[30] Figure 10 provides synoptic maps of GMI N<sub>2</sub>O from 70 to 90°N for 23–28 April, when the center of the FrIAC encroaches on the pole. For Eulerian advection simulations with a grid that is regularly spaced in latitude and longitude, the converging grids at the pole pose a challenging problem [Williamson, 2007]. In GMI, the mixing ratios are averaged over all longitudes for the grid cells closest to the poles (the “polar cap”) [Allen *et al.*, 1991]. This cap extends from 88.5 to 90°N for 1.00° latitude × 1.25° longitude grid. The mixing in the polar cap (identified by black circle) reduces

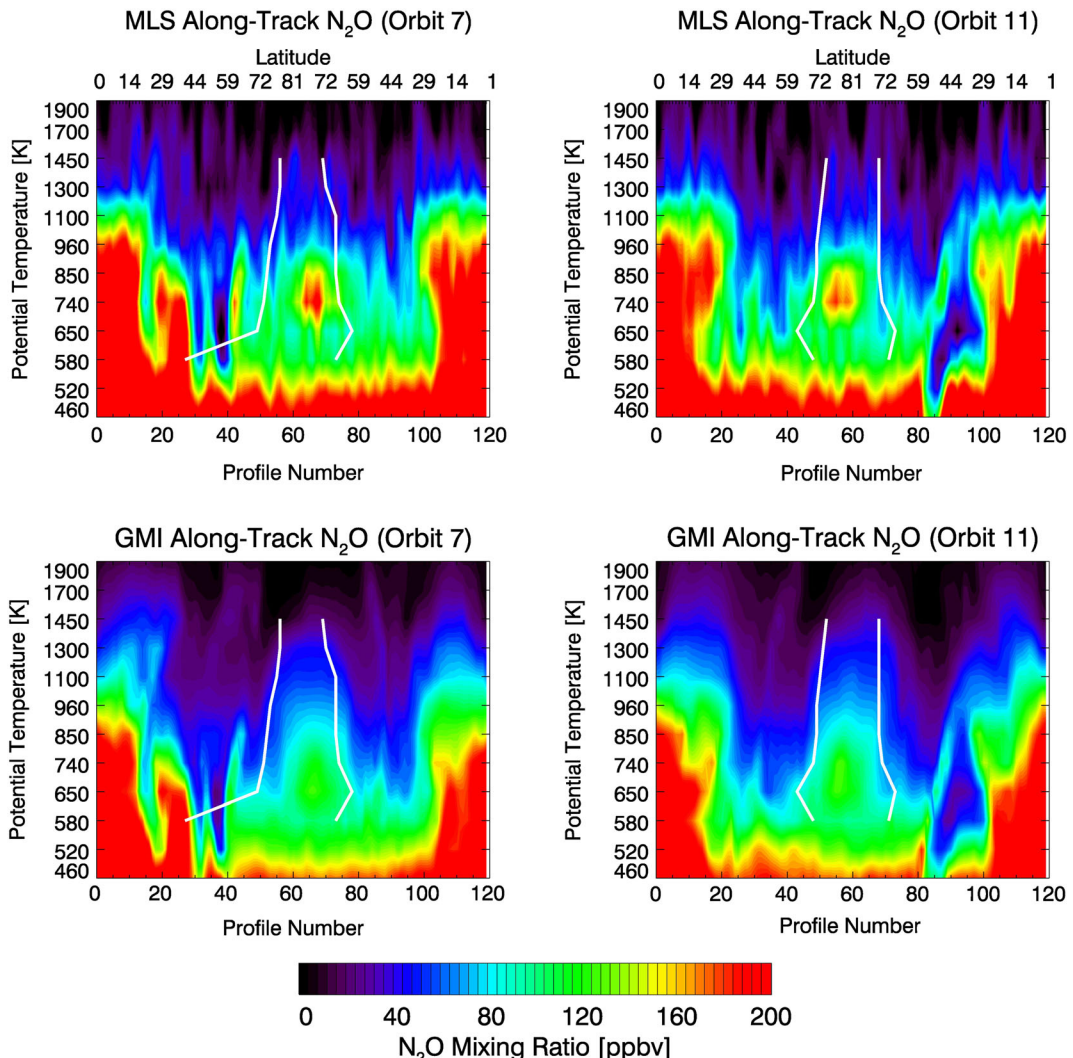


**Figure 9.** MLS and GMI curtain plots (along-track cross-section as function of potential temperature and profile number) for the two specified orbits from 21 April 2011 (see Figure 7). In all plots, red/blue contours indicate high/low N<sub>2</sub>O. White lines mark the edge of the anticyclone from 580 to 1450 K. The approximate latitude is provided on the top panels.

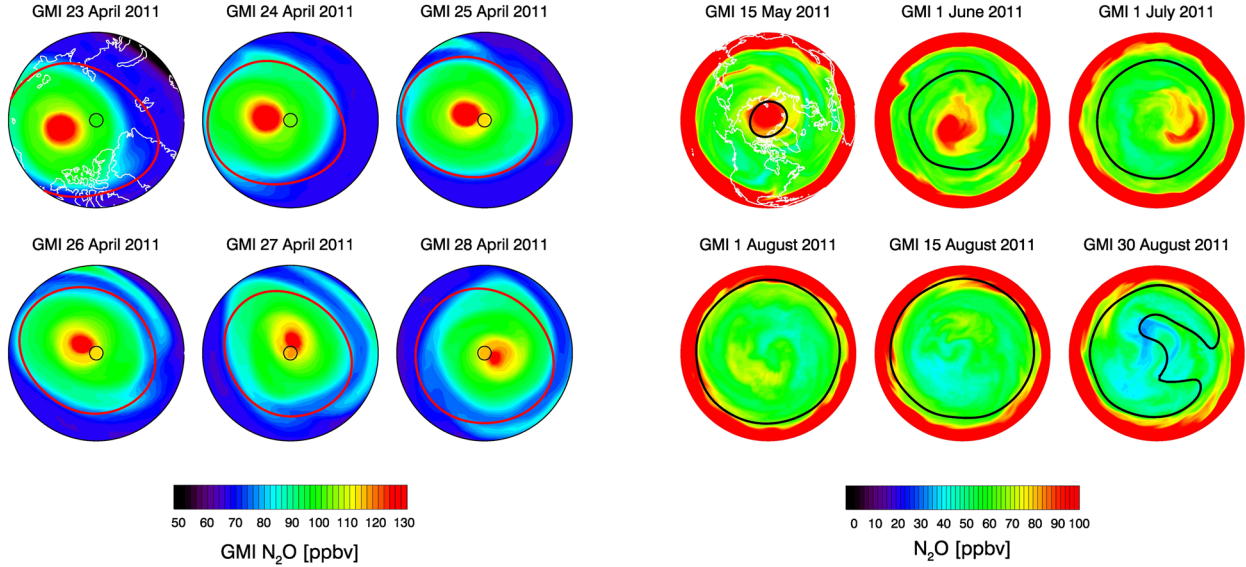


**Figure 10.** GMI  $\text{N}_2\text{O}$  mixing ratio from 70 to 90°N at 850 K (~32 km) for 23–28 April 2011. Black circles indicate the extent of the polar mixing cap. Red lines mark the edge of the anticyclone. In all plots, red/blue contours indicate high/low  $\text{N}_2\text{O}$ .

the areal extent of high  $\text{N}_2\text{O}$  values (red contours indicate values greater than ~120 ppbv) and reduces the peak mixing ratio by ~6.5%. A lower-resolution GMI simulation of this event (not shown) using a  $2.0^\circ \text{ latitude} \times 2.5^\circ \text{ longitude}$  grid results in a 17% reduction of the  $\text{N}_2\text{O}$  peak, which is similar to the 22% reduction observed in a similar GMI simulation of the 2005 FrIAC as it traversed the pole [Allen *et al.*, 2011]. For comparison, a VITA simulation, which was initialized with MLS  $\text{N}_2\text{O}$  data on 20 April 2011, advected the FrIAC over the pole from 20 April to 1 May with a decrease of only 0.6% in the peak value. Use of higher spatial resolution or alternate geometries, such as the cubed sphere or icosahedral grids, would likely perform better with this feature.

[31] The final demise of the  $\text{N}_2\text{O}$  anomaly associated with the FrIAC is illustrated in Figure 11, which shows synoptic maps of GMI  $\text{N}_2\text{O}$  at 850 K for select days in May through August 2011. During June through August, the polar region experiences horizontal and vertical wind shear that facilitates mixing of anomalies. As seen in June and July, the high- $\text{N}_2\text{O}$  air moves off the pole and becomes stretched and deformed from its original circular shape. During this process, the peak  $\text{N}_2\text{O}$  mixing ratio decreases significantly (for example, compare maps for 1 June and 1 August). The remnants of the FrIAC eventually vanish in late August, as the zonal winds reverse from easterly to westerly. The high  $\text{N}_2\text{O}$  at the pole is replaced by low  $\text{N}_2\text{O}$  values that will be incorporated into the developing winter polar vortex. The low  $\text{N}_2\text{O}$  values observed here are caused by a combination of polar descent from the diabatic circulation and photochemical processes (the photochemical loss rate is ~4–6 ppbv per month at 10 hPa in the summer polar region, 70–90°N). The MLS data (not shown) have a similar morphology to the GMI simulation, although the peak MLS  $\text{N}_2\text{O}$  values in the decaying FrIAC are slightly higher.

**Figure 11.** NH GMI  $\text{N}_2\text{O}$  at 850 K (~32 km) for select days from 15 May to 30 August 2011. Black lines mark the edge of the anticyclone. In all plots, red/blue contours indicate high/low  $\text{N}_2\text{O}$ .

[32] In addition to horizontal shear, significant vertical shear develops during this period. This is seen in Figure 1b, where isotachs that are vertically oriented (i.e., weak shear) in late May turn horizontal in June (strong shear). To illustrate the effects of the vertical shear on the  $\text{N}_2\text{O}$  distribution, we show longitude-height cross-sections of the GMI  $\text{N}_2\text{O}$  (deviation from the zonal mean) at 75°N in Figure 12 for select days in June and July. These plots use pressure as the vertical coordinate, incorporating the full GMI vertical resolution in order to resolve vertically fine-scale features. On 1 June, the positive  $\text{N}_2\text{O}$  anomaly is vertically upright, extending from approximately 30 to 2 hPa and roughly from 180° to 270° longitude. By 16 June, the positive anomaly has diminished in vertical range to ~20–5 hPa but is still basically upright, while the negative anomalies start to show a westerly tilt with increasing height. By 1 July, the tilting of the negative anomalies increases further and tilting is also seen in the positive anomaly. As the anomaly tilts, its vertical scale decreases, thereby enhancing vertical mixing processes. By 16 July, only a weak remnant of the positive anomaly remains at ~10 hPa and the vertical titling is even stronger. This mixing during the “shear phase” of the 2011 FrIAC is very similar to the 2005 FrIAC examined by Allen *et al.* [2011]. MLS data (not shown) are qualitatively similar, although the vertical resolution of MLS  $\text{N}_2\text{O}$  is ~4–6 km, compared to ~1–1.5 km for GMI, and therefore, some of the features are smoothed out in MLS.

## 5.2. Tracer Transport Using Vortex Edge Diagnostics

[33] The evolution of  $\text{N}_2\text{O}$  values that occur within the FrIAC at 850 K during the first 2 months from initial formation is provided in Figure 13a. The mean and range are given for MLS, GMI, and the VITA simulation initialized on 20 April. At the beginning of the time series, the range of GMI  $\text{N}_2\text{O}$  values in the FrIAC is quite large, with minimum and maximum of ~80 and 190 ppbv. Over time, the range narrows due to both confinement of the air in the anticyclone

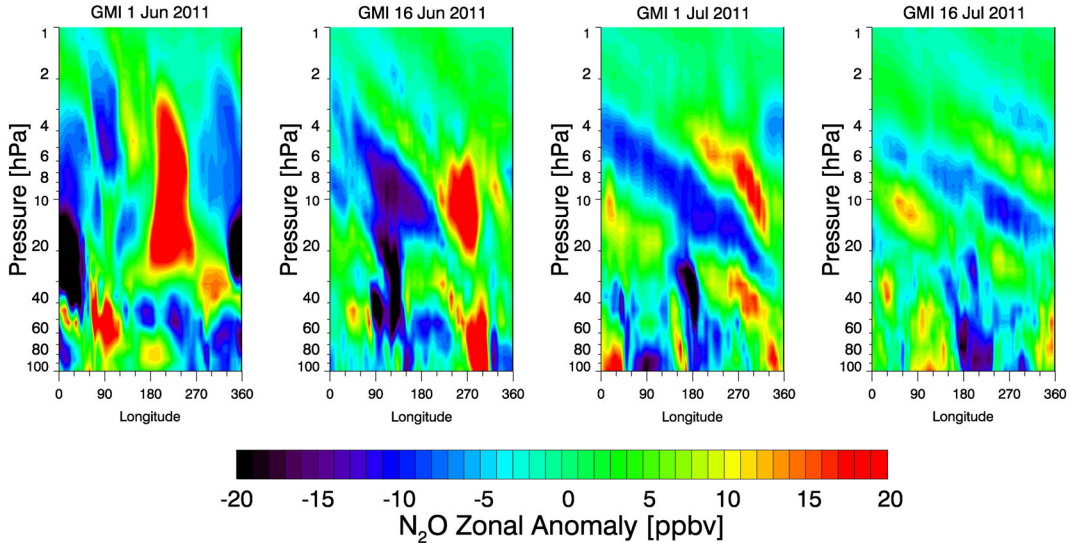


**Figure 12.** Pressure versus longitude cross-sections of GMI N<sub>2</sub>O (deviation from zonal mean) at 75°N latitude for 1 June, 16 June, 1 July, and 16 July. In all plots, red/blue contours indicate high/low N<sub>2</sub>O.

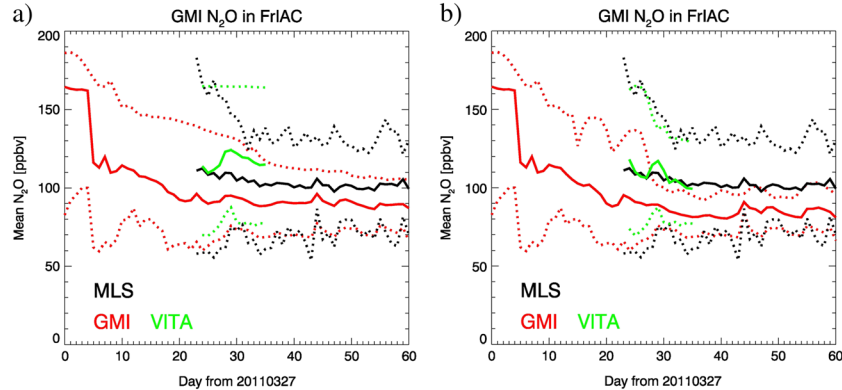


**Figure 13.** (a) Values of N<sub>2</sub>O within the FrIAC at 850 K (~32 km) from 27 March to 26 May 2011 as determined from (red) GMI, (black) MLS, and (green) VITA. The solid lines are the mean values within the FrIAC and the dotted lines are the minimum and maximum values. (b) Same as Figure 13a, except the sampling of the GMI and VITA data are limited to latitudes less than 82°N, to be consistent with the MLS sampling range.

as it speeds up and the subsequent local mixing within the anticyclone, which acts to homogenize the FrIAC air. After day 34 (April 30), the minimum and mean values are approximately constant in the GMI simulation, but the maximum continues to decrease slowly with time. The GMI simulation has a range of ~35 ppbv at the end of this period (26 May). The MLS data show a broad range of values on 20 April (day 24), with a peak that is considerably higher than in the GMI simulation. The peak MLS value drops sharply by 28 April (day 32). This is likely not due to actual mixing but is rather an artifact of the 82°S–82°N sampling range of the MLS instrument. As the central location of the FrIAC crosses the pole, MLS no longer measures the maximum N<sub>2</sub>O values within the FrIAC. This sampling bias is verified by the VITA simulation (initialized with MLS data on 20 April), which shows almost no reduction in the maximum N<sub>2</sub>O values within the FrIAC. In Figure 13b, the N<sub>2</sub>O values are sampled with the restriction that data north of 82°N (the limit of MLS sampling) were not

included. This allows the GMI and VITA outputs to be sampled over the same region as MLS. The VITA and MLS results agree quite well with this consistent sampling, suggesting that it is indeed the sampling bias that results in the steep drop in MLS maximum N<sub>2</sub>O values.

[34] Figure 14a presents probability distribution functions (PDFs) of the N<sub>2</sub>O mixing ratios at 850 K for air within the edge of the FrIAC. Plots are for select days from 27 March to 26 April 2011. The PDFs are derived for a range of N<sub>2</sub>O values from 50 to 200 ppbv, with a bin width of 5 ppbv. For the GMI and VITA simulations (red and green lines, respectively), the data are area weighted by grid size, while the MLS data (black lines) are not weighted, since each observation covers approximately the same area. All PDFs are normalized to their maximum value for each day. For the MLS PDFs, there is some ambiguity in determining whether the data are within the vortex edge. Since the MLS data are asynoptic, they can occur any time during the day, while the streamfunction used for this study is only

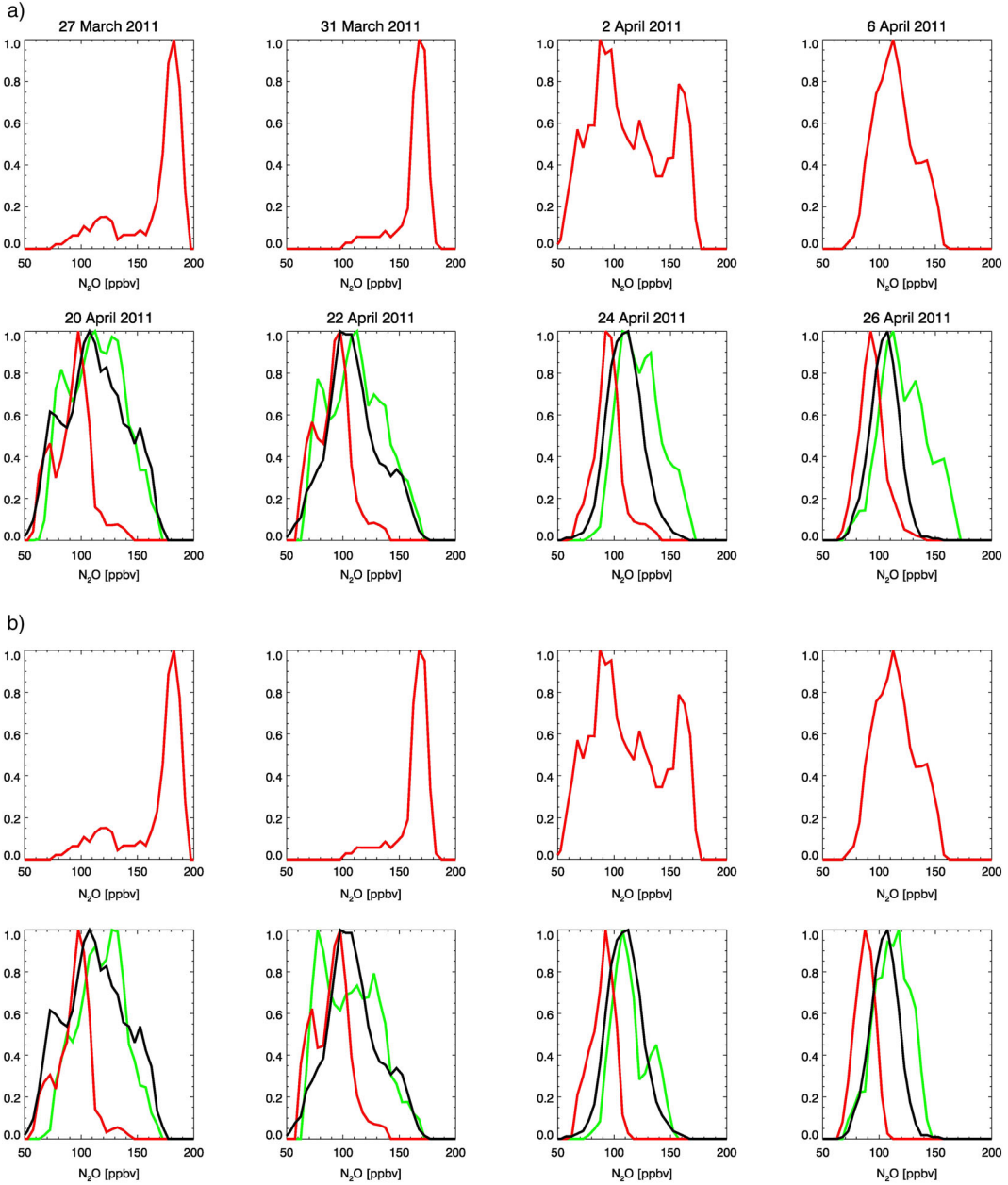


**Figure 14.** (a) Normalized PDFs of the  $\text{N}_2\text{O}$  values within the FrIAC at 850 K ( $\sim 32$  km) for select days from 27 March to 26 April 2011. Line colors are (red) GMI, (green) VITA, and (black) MLS. (b) Same as the second row of Figure 14a, except the sampling of the GMI and VITA data are limited to latitudes less than  $82^\circ\text{N}$ , to be consistent with the MLS sampling range.

available at analysis times (e.g., 12 Z is used here). One could in principle interpolate the streamfunction temporally to the time of the MLS measurement, but then, the edge value would also have to be calculated for each observation time. To simplify the analysis, we interpolated the 12 Z streamfunction spatially, but not temporally, to the MLS measurement locations and determined whether the interpolated value was inside or outside the FrIAC edge. There is therefore up to 12 Z difference between the streamfunction time and the MLS measurement time. It is unlikely that this difference adversely affects our conclusions, because during the time period of MLS analysis studied here (20–26 April),

the anticyclone was centered very close to the pole and did not change rapidly in either shape or position.

[35] On 27 March, the maximum GMI  $\text{N}_2\text{O}$  values are quite large, indicating air from the deep tropics. As the anticyclone moves eastward and poleward, the PDF shifts towards smaller  $\text{N}_2\text{O}$  values, and on 2 April, the PDF is quite broad, with two peaks centered near 80 and 150 ppbv. This indicates that the air enclosed by the anticyclone is changing character and the anticyclone is not simply transporting air intact (see also Figures 5e and 5f, where the PVEL and TrEL values jump to  $\sim 30^\circ$  around April 2). By 6 April, the range of  $\text{N}_2\text{O}$  values narrows considerably,

and over the next 2 weeks (6–20 April), the PDFs do not change shape significantly, although the ranges do narrow over this time. This suggests that the air in the FrIAC is isolated during this period and there is mixing within the FrIAC that is narrowing the range of values (this narrowing is also seen in the minimum/maximum values shown in Figure 13a).

[36] Starting on 20 April, the MLS data are available for comparison. MLS shows a much broader PDF (black line) on this date than the GMI simulation, particularly at the high N<sub>2</sub>O end of the distribution. From 20 to 26 April, the GMI PDF narrows slightly, with the higher N<sub>2</sub>O values being removed from the distribution. The MLS PDF narrows dramatically over this period, so that its shape is very similar to that of the GMI PDF by 26 April. The comparison is complicated by the fact that a portion of the FrIAC is becoming “hidden” from view of MLS as it crosses into the polar region, so the changes in the MLS PDF may be due to progressively incomplete sampling of the entire FrIAC, as suggested in Figure 13.

[37] To test this, we examine PDFs from the VITA model initiated on 20 April 2011. The VITA PDF (green line) on 20 April is slightly different from the MLS PDF due to the gridding procedure yet maintains the same basic shape. Over the next 6 days, while the MLS PDF narrows significantly, the VITA PDF narrows only slightly (note that the mixing is weak in the high-resolution VITA simulation). The differences are largely due to the MLS sampling pattern missing the largest N<sub>2</sub>O values in the core of the FrIAC. Therefore, the apparent good agreement between the shape of the GMI and MLS PDFs on 26 April is the fortuitous combination of the reduction of GMI maximum N<sub>2</sub>O values due to mixing in the polar region (as shown in section 5.1) and the “hiding” of the maximum N<sub>2</sub>O values from view of MLS since they occur near the pole. Since the FrIAC becomes permanently established at the pole, it is not possible to obtain MLS PDFs that sample the entire FrIAC after 20 April, so we cannot directly verify the VITA results. However, PDFs determined from excluding latitudes north of 82°N (Figure 14b) show a much closer agreement between VITA and MLS during this period, consistent with the results of Figure 13b.

## 6. Summary

[38] The winter-to-summer transition in the Arctic stratosphere involves a reversal of the polar vortex from westerly to easterly that is occasionally accompanied by a long-lived anticyclone that originates in the tropics and becomes embedded in the summer easterly flow. These FrIAC events transport low latitude air into the polar region, thereby affecting the chemistry of the summer vortex. The 2011 FrIAC was unusual in that the anticyclone that precipitated the FrIAC became permanently established at the pole and served as the “seed” for the developing easterly summer circulation. This was in contrast to the three previously examined FrIACs in 2003, 2005, and 2007, where the circulation anomaly appeared to be “frozen-in” to the ambient summer circulation. *Allen et al.* [2012] classified the 2011 event as a “large-scale FrIAC” to distinguish it from the other events. The spin-up of the 2011 FrIAC was detailed in this study by examining the synoptic evolution combined with a vortex

edge diagnostic based on relative rotation and shear of the horizontal wind. We examined the location, size, and flow of the FrIAC as well as the distributions of PVEL, TrEL, and N<sub>2</sub>O within the FrIAC. The vertical extent of the 2011 FrIAC was ~25 km (580–2100 K potential temperature) and the spatial size was ~75° in EL units. As the FrIAC moved poleward, the flow speed around the anticyclone edge increased and the air became more isolated from the extra-vortex air. The mean TrEL values remained relatively steady in April and May, while the PVEL values increased in most of the FrIAC due to diabatic processes. A small negative PVEL anomaly persisted until mid-June; the dynamics of this subsynoptic scale negative PV anomaly embedded in the summer circulation warrants further study.

[39] The tracer distribution within the FrIAC was analyzed with GMI and VITA simulations and MLS observations of N<sub>2</sub>O. The GMI simulation was able to capture many of the fine-scale features that were observed in MLS along-track cross-sections that occurred during the spin-up phase of the FrIAC. The VITA simulation showed additional filamentary structures that could not be resolved by GMI. When the VITA N<sub>2</sub>O was averaged vertically and horizontally to resemble the MLS resolution, there was good quantitative agreement with MLS data. High N<sub>2</sub>O filled the FrIAC and was maintained throughout the summer in both GMI and MLS. Mixing within the FrIAC was observed in the GMI simulations, with narrowing of the range of N<sub>2</sub>O values occurring at 850 K. The range of N<sub>2</sub>O values observed by MLS also narrowed, but this was largely due to the maximum N<sub>2</sub>O values within the FrIAC moving poleward of the maximum observing latitude (82°N). The peak GMI N<sub>2</sub>O mixing ratio dropped 6.5% when the center of the FrIAC encountered the pole, compared to less than 1% drop in VITA. This reduction was due to a polar cap mixing algorithm applied in the GMI advection scheme. The final demise of the 2011 FrIAC followed a similar course to the 2005 FrIAC, with horizontal and vertical shearing processes reducing the scales of the FrIAC and mixing the remnant high-N<sub>2</sub>O anomalies with the ambient low-N<sub>2</sub>O air.

## 7. Discussion

[40] The 2011 FrIAC provides an unusual geophysical experiment in which a coherent anticyclone travels from the subtropics to polar regions, displacing the polar vortex and establishing strong easterly winds. Although several FrIACs have now been examined in some detail, there are still a number of outstanding questions regarding FrIAC development and influence on the photochemistry of the summer vortex. For example, is it a coincidence that 2011 included both the coldest springtime on record and the most dramatic SFW, resulting in a record-breaking ozone loss as well as a highly unusual FrIAC event? *Thiéblemont et al.* [2011] argued that FrIAC occurrence is more likely in years with no major winter sudden stratospheric warming and with tropical quasi-biennial oscillation easterly phase. These were indeed both the case for 2011. However, additional factors are likely involved. The synoptic evolution of the 2011 FrIAC includes a precursor anticyclone over North America that may have preconditioned the rapid development of the FrIAC and the rapid demise of the winter vortex. Much insight could be gained by dynamical simulations of FrIACs

using GCMs, including whether GCMs produce FrIACs with the same properties and climatological frequency and whether GCMs show any trends in FrIAC occurrence associated with a changing climate.

[41] From a chemistry and transport modeling perspective, FrIACs can be used to test both the meteorological fields used to drive the model and the model's chemistry and transport schemes. The GMI CTM quantitatively simulates the long-lived tracer N<sub>2</sub>O during the entire lifecycle of the 2011 FrIAC, except for the low bias in the maximum values and anomalies that develop during the cross-polar flow. Simulations of these types of real-world events are a useful complement to the traditional idealized test cases employed to examine cross-polar transport capability in numerical advection schemes [e.g., Williamson *et al.*, 1992]. For example, in Søvde *et al.* [2012], simulations of cross-polar flow during the 2005 FrIAC event were used to document improvements made in the polar cap transport scheme used in the chemical transport model Oslo CTM3. Although we only examined one long-lived tracer, simulations of full stratospheric photochemistry accompanying the FrIAC also provide a useful method for validating and interpreting ground-based observations, as well as for validating the model photochemistry [Adams *et al.*, 2013].

[42] Diagnosing FrIAC properties is challenging in that the FrIAC is traveling, evolving, and interacting with other features of the flow. Using vortex edge diagnostics previously applied to LOP analysis, the FrIAC edge can be objectively identified, allowing isolation of air within the FrIAC. This approach would be very useful for a quantitative comparison of different FrIAC events. The analysis of Allen *et al.* [2012] showed a large amount of interannual variability in dynamics and tracer transport during the Arctic winter-to-summer transition with a number of FrIAC-like events being identified using the TrEL diagnostic. More detailed studies using GCM simulations and multidecadal reanalyses, combined with a vortex edge algorithm, would help to determine whether there are long-term trends in the frequency, strength, size, and composition of FrIACs.

[43] **Acknowledgments.** This work was supported by a subcontract from the NASA Atmospheric Composition: Modeling and Analysis Program, NNHH09ZDA001N. Work at the Naval Research Laboratory is sponsored by the Office of Naval Research. We would like to thank Gloria Manney for providing the gridded MLS data used to initialize the VITA simulations. We also acknowledge the Global Modeling and Assimilation Office and the Goddard Earth Science Data and Information Services Center for the dissemination of MERRA products.

## References

- Adams, C., et al. (2013), The spring 2011 final stratospheric warming above Eureka: Anomalous dynamics and chemistry, *Atmos. Chem. Phys.*, **13**, 611–624, doi: 10.5194/acp-13-611-2013.
- Allen, D. J., A. R. Douglass, R. B. Rood, and P. D. Guthrie (1991), Application of a monotonic upstream-biased transport scheme to three-dimensional constituent transport calculations, *Mon. Wea. Rev.*, **119**, 2456–2464.
- Allen, D. R., and N. Nakamura (2001), A seasonal climatology of effective diffusivity in the stratosphere, *J. Geophys. Res.*, **106**(D8), 7917–7935.
- Allen, D. R., and N. Nakamura (2002), Dynamical reconstruction of the record low column ozone over Europe on 30 November 1999, *Geophys. Res. Lett.*, **29**(9), 1362, doi:10.1029/2002GL014935.
- Allen, D. R., and N. Nakamura (2003), Tracer equivalent latitude: A diagnostic tool for isentropic transport studies, *J. Atmos. Sci.*, **60**(2), 287–304, doi:10.1175/1520-0469(2003)060<0287:TELADT>2.0.CO;2.
- Allen, D. R., R. M. Bevilacqua, G. E. Nedoluha, C. E. Randall, and G. L. Manney (2003), Unusual stratospheric transport and mixing during the 2002 Antarctic winter, *Geophys. Res. Lett.*, **30**(12), doi:10.1029/2003GL017117.
- Allen, D. R., A. R. Douglass, G. L. Manney, S. E. Strahan, J. C. Krosschell, J. V. Trueblood, J. E. Nielsen, S. Pawson, and Z. Zhu (2011), Modeling the frozen-in anticyclone in the 2005 Arctic summer stratosphere, *Atmos. Chem. Phys.*, **11**(9), 4557–4576, doi:10.5194/acp-11-4557-2011.
- Allen, D. R., A. R. Douglass, G. E. Nedoluha, and L. Coy (2012), Tracer transport during the Arctic stratospheric final warming based on a 33-year (1979–2011) tracer equivalent latitude simulation, *Geophys. Res. Lett.*, **39**, L12801, doi:10.1029/2012GL051930.
- Bancala, S., K. Kruger, and M. Giorgetta (2012), The preconditioning of major sudden stratospheric warmings, *J. Geophys. Res.*, **117**, D04101, doi:10.1029/2011JD016769.
- Bey, I., D. J. Jacob, R. M. Yantosca, J. A. Logan, B. D. Field, A. M. Fiore, Q. B. Li, H. G. Y. Liu, L. J. Mickley, and M. G. Schultz (2001), Global modeling of tropospheric chemistry with assimilated meteorology: Model description and evaluation, *J. Geophys. Res.*, **106**(D19), 23,073–23,095.
- Charney, J. G., and P. G. Drazin (1961), Propagation of planetary-scale disturbances from lower into upper atmosphere, *J. Geophys. Res.*, **66**(1), 83–109.
- Douglass, A. R., R. S. Stolarski, S. E. Strahan, and P. S. Connell (2004), Radicals and reservoirs in the GMI chemistry and transport model: Comparison to measurements, *J. Geophys. Res.*, **109**, D16302, doi:10.1029/2004JD004632.
- Fairlie, T. D. (1995), Three-dimensional transport simulations of the dispersal of volcanic aerosol from Mount Pinatubo, *Q. J. Roy. Meteor. Soc.*, **121**(528), 1943–1980.
- Fairlie, T. D., R. B. Pierce, J. A. Al-Saadi, W. L. Grose, J. M. Russell, M. H. Proffitt, and C. R. Webster (1999), The contribution of mixing in Lagrangian photochemical predictions of polar ozone loss over the Arctic in summer 1997, *J. Geophys. Res.*, **104**(D21), 26,597–26,609.
- Harvey, V. L., R. B. Pierce, T. D. Fairlie, and M. H. Hitchman (2002), A climatology of stratospheric polar vortices and anticyclones, *J. Geophys. Res.*, **107**(D20), 4442, doi:10.1029/2001JD001471.
- Harvey, V. L., R. B. Pierce, M. H. Hitchman, C. E. Randall, and T. D. Fairlie (2004), On the distribution of ozone in stratospheric anticyclones, *J. Geophys. Res.*, **109**, D24308, doi:10.1029/2004JD004992.
- Harvey, V. L., C. E. Randall, G. L. Manney, and C. S. Singleton (2008), Low-ozone pockets observed by EOS-MLS, *J. Geophys. Res.*, **113**, D17112, doi:10.1029/2007JD009181.
- Haynes, P. H. (1990), High-resolution three-dimensional modeling of stratospheric flows: Quasi-two-dimensional turbulence dominated by a single vortex, in *Topological Fluid Mechanics*, edited by H. K. Moffat, and A. Tsinober, pp. 354–354, Cambridge Univ. Press, New York.
- Hess, P. (1990), Variance in trace constituents following the final stratospheric warming, *J. Geophys. Res.*, **95**(D9), 13,765–13,779.
- Hess, P. G. (1991), Mixing processes following the final stratospheric warming, *J. Atmos. Sci.*, **48**(14), 1625–1641.
- Hurwitz, M. M., P. A. Newman, and C. I. Garfinkel (2011), The Arctic vortex in March 2011: A dynamical perspective, *Atmos. Chem. Phys.*, **11**, 11,447–11,453, doi:10.5194/acp-11-11447-2011.
- Lahoz, W. A., A. J. Geer, and Y. J. Orsolini (2007), Northern Hemisphere stratospheric summer from MIPAS observations, *Q. J. Roy. Meteor. Soc.*, **133**, 197–211, doi:10.1002/qj.24.
- Lambert, A., et al. (2007), Validation of the Aura Microwave Limb Sounder middle atmosphere water vapor and nitrous oxide measurements, *J. Geophys. Res.*, **112**, D24S36, doi:10.1029/2007JD008724.
- Lin, S. J., and R. B. Rood (1996), Multidimensional flux-form semi-Lagrangian transport schemes, *Mon. Weather. Rev.*, **124**(9), 2046–2070.
- Livesey, N. J., et al. (2011), Earth Observing System (EOS) Aura Microwave Limb Sounder (MLS) Version 3.3 Level 2 data quality and description document, *JPL D-33509*, 162 pp.
- Manney, G. L., N. J. Livesey, C. J. Jimenez, H. C. Pumphrey, M. L. Santee, I. A. MacKenzie, and J. W. Waters (2006), EOS Microwave Limb Sounder observations of “frozen-in” anticyclonic air in Arctic summer, *Geophys. Res. Lett.*, **33**, L06810, doi:10.1029/2005GL025418.
- Manney, G. L., et al. (2011), Unprecedented Arctic ozone loss in 2011, *Nature*, **478**(7370), 469–475, doi:10.1038/nature10556.
- McIntyre, M. E., and T. N. Palmer (1983), Breaking planetary-waves in the stratosphere, *Nature*, **305**(5935), 593–600.
- Orsolini, Y. J. (2001), Long-lived tracer patterns in the summer polar stratosphere, *Geophys. Res. Lett.*, **28**(20), 3855–3858.
- Piani, C., and W. A. Norton (2002), Solid-body rotation in the Northern Hemisphere summer stratosphere, *Geophys. Res. Lett.*, **29**(23), 2117, doi:10.1029/2002GL016079.
- Rienecker, M. M., et al. (2011), MERRA: NASA’s modern-era retrospective analysis for research and applications. *J. Climate*, **24**(14), 3624–3648, doi:10.1175/JCLI-D-11-00015.1.
- Schoeberl, M. R., A. R. Douglass, R. S. Stolarski, S. Pawson, S. E. Strahan, and W. Read (2008), Comparison of lower stratospheric

- tropical mean vertical velocities, *J. Geophys. Res.*, 113, D24109, doi:10.1029/2008JD010221.
- Schwartz, M. J., et al. (2008), Validation of the Aura Microwave Limb Sounder temperature and geopotential height measurements, *J. Geophys. Res.*, 113, D15S11, doi:10.1029/2007JD008783.
- Søvde, O. A., et al. (2012), The chemical transport model Oslo CTM3, *Geosci. Model Dev.*, 5, 1441–1469, doi:10.5194/gmd-5-1441-2012.
- Strahan, S. E., B. N. Duncan, and P. Hoor (2007), Observationally derived transport diagnostics for the lowermost stratosphere and their application to the GMI chemistry and transport model, *Atmos. Chem. Phys.*, 7, 2435–2445, doi:10.5194/acp-7-2435-2007.
- Strahan, S. E., et al. (2011), Using transport diagnostics to understand chemistry climate model ozone simulations, *J. Geophys. Res.*, 116, D17302, doi:10.1029/2010JD015360.
- Thiéblemont, R., N. Huret, Y. J. Orsolini, A. Hauchecorne, and M. A. Drouin (2011), Frozen-in anticyclones occurring in polar Northern Hemisphere during springtime: Characterization, occurrence and link with quasi-biennial oscillation, *J. Geophys. Res.*, 116, D20110, doi:10.1029/2011JD016042.
- Waters, J. W., et al. (2006), The Earth Observing System Microwave Limb Sounder (EOS MLS) on the Aura satellite, *IEEE T. Geosci. Remote*, 44 (5), 1075–1092, doi:10.1109/Tgrs.2006.873771.
- Wei, K., W. Chen, and R. H. Huang (2007), Dynamical diagnosis of the breakup of the stratospheric polar vortex in the Northern Hemisphere, *Sci. China Ser. D*, 50(9), 1369–1379, doi:10.1007/s11430-007-0100-2.
- Williamson, D. L. (2007), The evolution of dynamical cores for global atmospheric models, *J. Meteor. Soc. Japan*, 85B, 214–269, doi:10.2151/jmsj.85B.241.
- Williamson, D. L., J. B. Drake, J. J. Hack, R. Jakob, and P. N. Swarztrauber (1992), A standard test set for numerical approximations to the shallow-water equations in spherical geometry, *J. Comput. Phys.*, 102(1), 211–224.